Tailoring very-high-n circular wave packets

C. O. Reinhold,[1,2] S. Yoshida,[3] J. Burgdörfer,[2,3] J. J. Mestayer,[4] B. Wyker,[4] J. C. Lancaster,[4] and F. B. Dunning[4]

[1]*Physics Division, Oak Ridge National Laboratory, Oak Ridge, Tennessee 37831-6372, USA*
[2]*Department of Physics, University of Tennessee, Knoxville Tennessee 37996, USA*
[3]*Institute for Theoretical Physics, Vienna University of Technology, Vienna, Austria, EU*
[4]*Department of Physics and Astronomy and the Rice Quantum Institute, Rice University, Houston, Texas 77005-1892, USA*

We describe a protocol to generate transiently localized circular wave packets in very-high-n Rydberg states. These are created from strongly polarized quasi-one-dimensional Rydberg states by applying a transverse pulsed electric field. The resulting wave packet becomes transiently localized as the result of focusing and travels in a nearly circular Bohr-like orbit around the nucleus for several orbital periods. The localization properties can be controlled by carefully choosing the shape of the field pulse, in particular, its rise and fall times. Remarkably, the wave packets exhibit classical revivals after the initial dephasing on time scales shorter than those expected for quantum revivals.

I. INTRODUCTION

Controlling and manipulating the electronic states of microscopic and mesoscopic systems is an active field of research. Atoms in high-lying Rydberg states with large values of principal quantum number n provide a valuable mesoscopic system in which to explore such control. Various techniques have been devised to create different stationary Rydberg states including stationary circular states where the electron is placed in a state with extremely high values of one component of the angular momentum $\langle L_i \rangle \sim \pm (n-1)\hbar$ [1–5]. Interest in circular states stems from their unique dynamical properties. The high centrifugal barrier keeps the electron far away from the (nonhydrogenic) core resulting in their remarkable stability. Radiative transitions are effectively limited to $\Delta n = \pm 1$, which is exploited in cavity-quantum electrodynamics studies [6].

The development of ultrafast electromagnetic pulses has opened up the possibility of engineering "nonstationary" Rydberg states, i.e., wave packets. Techniques for producing and probing Rydberg wave packets have become feasible only recently [7–10] using pulses whose time scales are smaller than the electron Kepler period, $T_n = 2\pi n^3$ (atomic units are used throughout). Transiently localized wave packets that move in near-circular orbits and resemble a quasiclassical electron moving in a Bohr-like orbit are difficult to produce experimentally and have principally been the object of theoretical study [11,12]. However, we recently reported the experimental realization of such "Bohr-like" wave packets in very-high-n ($n=306$) Rydberg atoms [13]. The formation of these wave packets was based on a multistep protocol. Initially, stationary quasi-one-dimensional (quasi-1D) Rydberg atoms strongly oriented along a given axis (the $+x$ axis) are created [14]. A transverse "pump" electric field pulse is then rapidly applied along a perpendicular axis (the z axis). This creates a Stark wave packet [15,16] that undergoes periodic changes in its y component of angular momentum, L_y. Rapidly switching off the "pump" field prevents further evolution in L_y creating a wave packet with a well-defined eccentricity. By carefully choosing the duration of

the pump pulse a nearly circular wave packet can be realized traveling clockwise (or anticlockwise) in the xz plane that subsequently localizes in azimuth to form a Bohr-like state.

Here we present a detailed analysis of the wave-packet dynamics underlying this protocol using both theory and experiment. We demonstrate that the observed localization of the wave packet is associated with classical focusing near caustics. Moreover, we find this focusing to be remarkably sensitive to the shape and the fall time of the pump pulse which control the spread in energy (or n) of the wave packet. Under appropriate conditions classical revivals of the wave packets are observed which are to be distinguished from the well-known quantum revivals seen for lower n. The classical revivals appear on shorter time scales than their quantum counterparts and are therefore easier to observe with very high n, $n \sim 300$, atoms where the quantum revival time $T_R \simeq n T_n / 3$ is ~ 440 ns.

II. THEORY

The principles underlying the present protocol can be illustrated by following the evolution of a single elongated Coulomb orbit when exposed to an electric pump pulse F_z^{pump}. The dynamics of the electron is governed by the Stark Hamiltonian

$$H^{\text{Stark}}(t) = H^{\text{at}} + z F_z^{\text{pump}}(t) = \frac{p^2}{2} - \frac{1}{r} + z F_z^{\text{pump}}(t), \quad (1)$$

where $\vec{r}=(x,y,z)$ and $\vec{p}=(p_x,p_y,p_z)$ are its coordinate and momentum, respectively, and H^{at} is the free-atom Hamiltonian. To first order in F_z^{pump}, the angular momentum $\vec{L}=\vec{r} \times \vec{p}$, and the Runge-Lenz vector $\vec{A}=\vec{p} \times \vec{L} - (1/r)\vec{r}$ precess about the pump field, i.e., the z axis, following the Bloch equations [17,18],

$$\frac{d}{dt}(\vec{L} \pm n\vec{A}) \simeq \frac{\pm \omega_S(t)}{2}(\vec{L} \pm n\vec{A}) \times \hat{z}, \quad (2)$$

where $n=1/\sqrt{-2H_{\text{at}}}$ and $\omega_S(t)=3nF_z^{\text{pump}}(t)$ is the Stark frequency which coincides with the energy splitting between
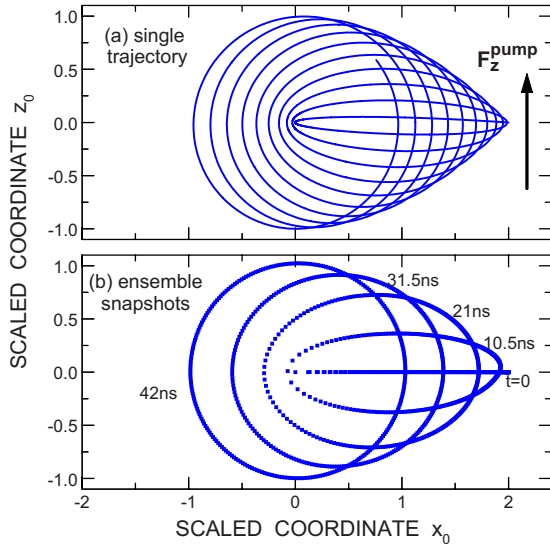
FIG. 1. (Color online) Time evolution of a Rydberg electron initially in a linear $n_i = 306$ 1D state oriented along the x axis in a field $F_z^{pump} = -10$ mV cm^{-1} that is suddenly turned on at $t = 0$ and is directed along the z axis. (a) Time evolution of a single classical trajectory. (b) Snapshots of the ensemble of trajectories originating at $t = 0$ on the 1D state with random Kepler time τ (see text). The various snapshots are taken at the times indicated which extend to one-half of the Stark precession period $T_S/2 \sim 42.5$ ns. Scaled units $x_0 = x/n_i^2$ and $z_0 = z/n_i^2$ are used.

adjacent quantum Stark states. To simplify the discussion we first consider the evolution of a Coulomb orbit in a fixed (time-independent) field. The z components of both $\vec{L}$ and $\vec{A}$, L_z and A_z, are constants of motion while the dynamics of the other components, L_x, L_y, A_x, A_y, resemble that of a harmonic oscillator. For example, if at $t = 0$ $\vec{A}$ and $\vec{L}$ are parallel to the x and y axes, respectively, the Bloch equation [Eq. (2)] has the solution

$$\vec{A} = -\hat{x}\cos(\omega_S t/2), \quad \vec{L} = \hat{y}n\sin(\omega_S t/2). \quad (3)$$

This precessional motion is illustrated in Fig. 1 for an electron with principal action (or quantum number) $n_i = 306$ initially in an $L = 0$ Kepler ellipse represented by a line oriented along the positive x axis ($\vec{A} = -\hat{x}$). We refer to this classical initial "orbit" as a "one-dimensional" (1D) state to highlight its similarity to states used in reduced-dimension models. The latter have been shown to capture the essential physics of elongated parabolic states with large electric dipole moments. We emphasize that the dynamics in the present description is fully three dimensional and that the simulations of the experiments employ realistic three-dimensional ensembles. As shown in Fig. 1(a), if such a 1D state is suddenly exposed to a pump field $F_z^{pump} = -10$ mV/cm along the z axis, i.e., a scaled field $|F_0| = n_i^4 |F_z^{pump}| = 0.017$, the orbit begins to precess and change its shape. The dynamics proceeds in the xz plane ($y = p_y = 0$, $A_z = L_z = 0$). The electron orbit (orbital period $T_{n_i} = 2\pi n_i^3 = 4.3$ ns) changes from being highly elliptic to being nearly circular ($L_y \simeq -n_i$) on a time scale of one-half a Stark period $T_S/2 \sim \pi/(3n_i|F_z^{pump}|) \sim 42.5$ ns [one-quarter of

the precession period in Eq. (3)]. The key to the present protocol is that by suddenly switching off the pump field at $t = t_{off} = T_S/2$ further evolution of the orbit is halted leaving the electron moving counterclockwise in a nearly circular orbit.

Another important factor in the success of the present protocol is that electron trajectories starting at different positions on the initial orbit (usually expressed by their "mean anomalies" or Kepler times τ) end up in nearly the same circular orbit at approximately the same time $T_S/2$. Consider a distribution of initial conditions sampled from a microcanonical ensemble with well-defined angular momentum $L \simeq 0$ and Runge-Lenz vector $\vec{A} \simeq -\hat{x}$ using a classical trajectory Monte Carlo (CTMC) approach [19]. As seen in Fig. 1(b), while the initial density of points is largest near the outer turning point (the apocenter) where the electron moves slowest, the final density of points at $t = T_S/2$ is nearly uniformly distributed around a circle reflecting the fact that electrons in circular orbit travel with a constant velocity. However, what is not evident from Fig. 1(b) is that the ensemble created after turn off of the pump pulse is nonstationary, i.e., a wave packet. As will be discussed, this results from small position-dependent changes in the electron energy associated with the (sudden) turn off of the pump field which translates into a position dependence in the subsequent orbital frequencies, $\omega(\phi_i) = n(\phi_i)^{-3}$. When that part of the ensemble orbiting at the higher frequencies catches up with that part orbiting more slowly the ensemble becomes transiently localized forming a Bohr-like wave packet in a nearly circular orbit [13].

The time evolution of the ensemble can be made more explicit by examining the time evolution of the angular probability density $\rho(\phi)$, where ϕ is the azimuthal angle, i.e., $\phi = \arctan(z/x)$. This is displayed in Fig. 2(a) as a function of time after turn off of the pump pulse. In the following, the scaled variables (denoted by a subscript 0) $x_0 = x/n_i^2$, $p_0 = n_i p$, and $t_0 = t/(2\pi n_i^3) = t/T_{n_i}$ are used. The essential dynamics occurs in the azimuthal degree of freedom which depends linearly on time,

$$\phi(t) = \phi_i + \omega(\phi_i)(t - t_{off}), \quad (4)$$

where t_{off} corresponds to the time at which the pump field was switched off. Each electron with an initial azimuthal angle ϕ_i has a unique angular velocity $\omega(\phi_i)$. Note that for circular orbits the azimuthal angle is identical to the mean anomaly of the Kepler orbit.

The behavior of the mean value of the azimuthal angle is shown, on a longer time scale, in Fig. 2(b). It too depends linearly on time as $\langle\phi\rangle = \langle\phi_i\rangle + \langle\omega\rangle(t - t_{off})$, where $\langle\omega\rangle \simeq \omega_{n_i} = n_i^{-3}$. [Mapping ϕ onto the principal branch $[-\pi, \pi]$ (or its first Brillouin zone) gives rise to the apparent discontinuous behavior seen in Fig. 2(b)]. As evident from Figs. 2(a) and 2(c), the width of the angular distribution, i.e., its standard deviation, $\Delta\phi$, exhibits successive minima indicating that the wave packet periodically localizes in ϕ. The smallest value of $\Delta\phi$, which corresponds to optimal localization, is reached at $t_L \approx 6T_{n_i}$, i.e., six orbital periods after turn off of the pump field, when its width $\langle\Delta\phi\rangle$ is reduced to $\lesssim 1$ radian. There-
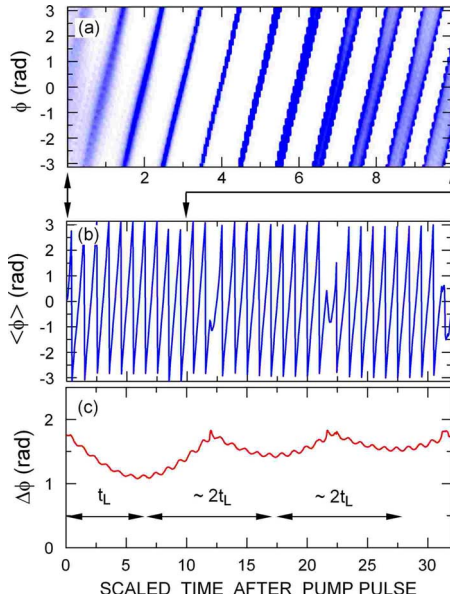
FIG. 2. (Color online) Time evolution following sudden turn off of the pump field for (a) the azimuthal angular distribution of the wave packet, (b) the average value of the azimuthal angle, and (c) the width of the angular distribution (see text). The initial state is the $n_i=306$ 1D state as in Fig. 1 and the pump pulse has a peak field of -10 mV cm^{-1} and a duration of 42.5 ns. The scaled time after turn off of the pump pulse is $t_0=(t-t_{off})/T_{n_i}=(t-t_{off})/(2\pi n_i^3)$. The azimuthal angles are measured from the $+x$ axis. Note that the time scale in the upper frame is different from that of the lower two frames.

after, the wave packet dephases but periodically rephases at times $t_{rev}^{(i)}=(2i+1)t_L$, $(i=0,1,\dots)$. We refer to this periodic relocalization as "classical" revivals. (These are to be distinguished from quantum revivals which occur on much longer time scales.) The localization at successive classical revivals, however, becomes less pronounced, i.e., the width $\langle\Delta\phi\rangle_i$ increases with i.

For any particular electron trajectory, the x and z coordinates are given by

$$(x(t),z(t)) \simeq n^2(\cos\phi(t),\sin\phi(t)) \qquad (5)$$

and are 90° out of phase from each other. The time dependence of the expectation values of the x and z coordinates of the ensemble are shown in Figs. 3(a) and 3(b). Their behaviors approximately mirror that predicted by Eq. (5) exhibiting fast oscillations with the average Kepler frequency. However, the amplitudes of the oscillations are modulated and follow the behavior of the width, $\Delta x\Delta z$, of the wave packet in the xz plane, shown in Fig. 3(c), or the angular width [see Fig. 2(c)].

The classical localization of the wave packet following the pump pulse is a consequence of focusing of the classical ensemble. This can be understood by analyzing the focal points (caustics) of the system [20]. The search for focal points is greatly simplified when considering an initial 1D state. The "location" of the electron within the initial linear orbit can be characterized by the Kepler time, τ, immediately before application of the pump pulse (at $t=0$). The Kepler
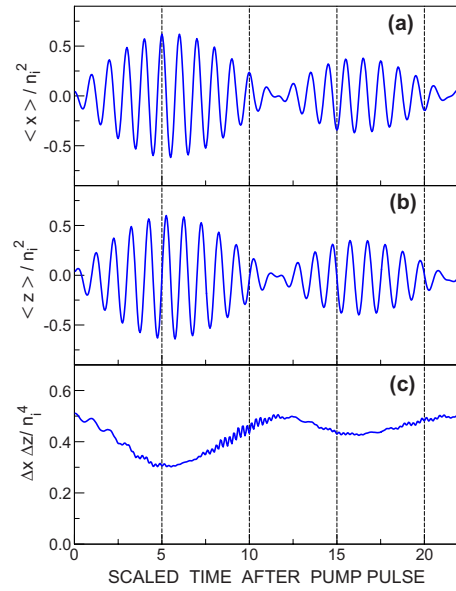
FIG. 3. (Color online) Time evolution following sudden turn off of the pump field for (a) the expectation value of x, (b) the expectation value of z, and (c) the width of the wave packet in the xz plane given by the product of the widths (standard deviations) in x and z. The initial state is the $n_i=306$ 1D state as in Fig. 1. The pump pulse has a peak field of -10 mV cm^{-1} and a duration of 42.5 ns.

time is defined by the implicit Kepler equations $\tau=n_i^3(\xi-\sin\xi)$ and $x=n_i^2(1-\cos\xi)$ with $-1/2<\tau/T_{n_i}<1/2$. (τ is proportional to the angle variable conjugate to the principal action n_i and referred to as the "mean anomaly." In turn, ξ is called the eccentric anomaly.) In the absence of the pump pulse the principal action n is a constant of motion, the electron motion being effectively one-dimensional and described by the time evolution of $x(t)$ for the linear orbit. For the circular orbit into which the linear orbit evolves, the relevant variable is $\phi(t)$. The time evolution of the azimuthal angle (or any other variable) is characterized by a unique function $\phi(t,\tau)$ of time and the initial position in the orbit, τ. The angular probability density at a time t is given by

$$\rho(\phi,t) = \sum \rho(\tau)\left|\frac{\partial\phi}{\partial\tau}\right|^{-1} = \mathrm{const}\sum\left|\frac{\partial\phi}{\partial\tau}\right|^{-1}, \qquad (6)$$

where $|\partial\phi/\partial\tau|$ is the Jacobian of the transformation and the sum extends over all the initial values of τ leading to the same final value of $\phi\in[-\pi,\pi]$. For an initial stationary microcanonical ensemble the probability density of the intrinsic time is uniform, i.e., $\rho(\tau)=\mathrm{const}$ [19]. The distribution function $\rho(\phi,t)$ is therefore simply given by the Jacobian of the transformation. In particular, zeros of the Jacobian (i.e., $|\partial\phi/\partial\tau|=0$) represent focal points and lead to singular behavior in $\rho(\phi,t)$.

Figure 4 illustrates the behavior of the function $\phi(t,\tau)$ at selected times following turn off of the pump pulse (in contrast to Fig. 2, the azimuthal angle is not reduced to the $[-\pi,\pi]$ interval). At the end of the pump pulse, i.e., at $t=t_{off}$, the azimuthal angle has a linear dependence $\phi/\pi\sim 2\tau/T_{n_i}$+const, leading to the nearly uniform distribution visible in
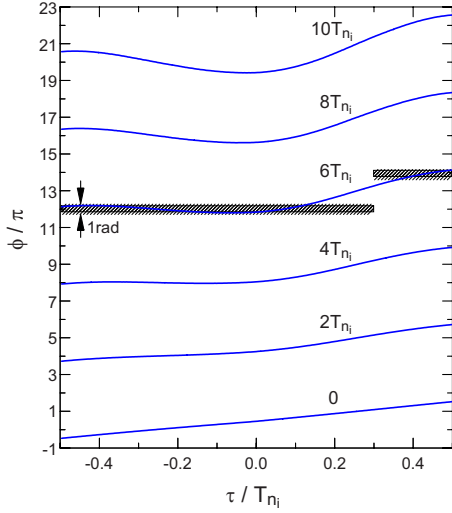
FIG. 4. (Color online) Evolution of the azimuthal angle $\phi(\tau,t)$ as a function of the Kepler time τ for the selected times $(t-t_{off})$ indicated following turn off of the pump field. The shaded horizontal region for $(t-t_{off})=6T_{n_i}$ encompasses about 80% of the wave packet which is focused within an angular width of $\sim$1 rad (the apparent discontinuity can be removed by a transformation modulo 2π).

Figs. 1 and 2. For several orbital periods after turn off of the pump field $\phi(t,\tau)$ is a monotonic function of τ until it develops an inflection point at $(t-t_{off})\sim4T_{n_i}$ [both the first and second derivatives of $\phi(t,\tau)$ vanish]. At later times the function $\phi(t,\tau)$ develops both a maximum and a minimum and, therefore, $|\partial\phi/\partial\tau|=0$ at two values τ_1, and τ_2, which persist for all times. The point of maximum localization occurs at $t\sim6T_{n_i}$ as the inflection point splits into a maximum and a minimum (i.e., when τ_1 and τ_2 separate from each other). About 80% of the wave packet is focused within an angular range of $\lesssim$1 rad (denoted by the shaded area in the figure). At later times the probability density develops two peaks as seen in Fig. 2(a), which are directly related to the maxima and minima of $\phi(t,\tau)$.

The characteristic properties of this classical phase-space distribution (or wave packet) are directly related to the probability densities $\rho(E)$ and $\rho(L_y)$ for the binding energy $E \equiv H^{at}$ and the y component of the angular momentum L_y created by the pump field. As for the angular probability density $\rho(\phi,t)$ [Eq. (6)], $\rho(E)$ and $\rho(L_y)$ are given directly by the functions $E(t,\tau)$ and $L_y(t,\tau)$ displayed in Fig. 5. In contrast to $\phi(t,\tau)$, these functions are time independent after the pump field is turned off, i.e., $E(t,\tau)=E(t_{off},\tau)$ for $t>t_{off}$. The final ensemble of points encompasses a narrow range of energies (corresponding to $301<n<311$) and angular momenta $(-311<L_y<-300)$. In addition, $E(t_{off},\tau)$ and $L_y(t_{off},\tau)$ have a maximum and a minimum and, consequently, focal points. The corresponding energy distribution is displayed in Fig. 6 and is characterized by two peaks (square root singularities associated with the minima and maxima in Fig. 5) separated by the energy difference ΔE. The mean binding energy of the wave packet $\langle E\rangle\sim E_{n_i}$ is associated with the fast oscillation evident in Figs. 3(a) and 3(b) while the width ΔE determines the frequency of the
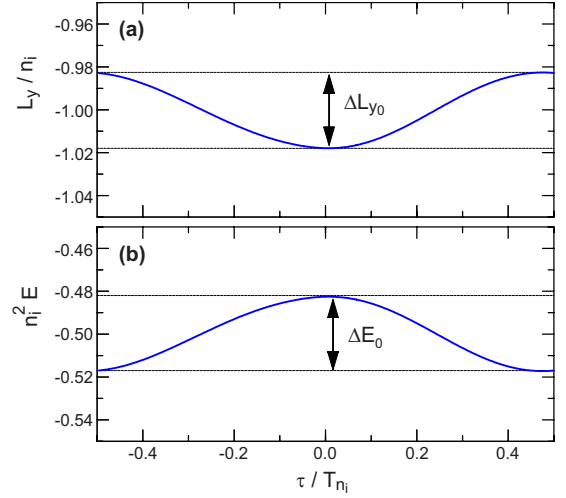
FIG. 5. (Color online) Angular momentum (a) and energy (b) of electrons in the ensemble in Fig. 1(b) after the pump field is turned off at t_{off}=42.5 ns as a function of the mean anomaly or Kepler time τ of the initial orbit.

amplitude modulation and the localization times.

The transient localization of the wave packet results because, following turn off of the pump field, phase points, i.e., electrons, at different points around the orbit rotate with slightly different Kepler frequencies ω, determined by the binding energy through, $\omega=(-2E)^{3/2}$. As will be explained later, points near the maximum energy (n=311) are initially located on the opposite side of the orbit to those points with near the minimum energy (n=301) and have smaller angular velocity. Focusing occurs as the faster moving (lower-n) phase-space points catch up with the slower-moving (higher-n) points. Since these groups of phase points are initially separated by an azimuthal angle of $\Delta\phi\approx\pi$, the first localization time can be estimated from the condition

$$\Delta\omega t_L = \{(-2E_{min})^{3/2} - [-2(E_{min}+\Delta E)]^{3/2}\}t_L = \pi. \quad (7)$$

To first order in $\Delta E/E_{n_i}$ this leads to
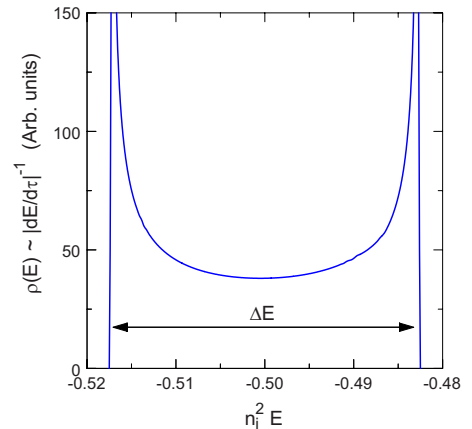
FIG. 6. (Color online) Energy distribution $\rho(E)\propto|dE/d\tau|^{-1}$ of the wave packet after the pump field is turned off at $t_{off}=T_S/2$ =42.5 ns, corresponding to the function $E(\tau)$ in Fig. 5.

$$t_L/T_{n_i} \simeq \frac{1}{6n_i^2 \Delta E}, \tag{8}$$

which approximately agrees with the values obtained using numerical calculations. Localization is then lost but is subsequently recovered when the fastest phase points overlap with the slowest phase points for the second time, third time, etc., giving rise to classical revivals at times $t_{rev} = (2i+1)t_L$. These revivals are due to the finite width ΔE of the final electron energy distribution which, as shown in Fig. 6, has sharp cutoffs at E_{min} and E_{max} and is strongly peaked at its extremes due to the focal points in $\rho(E)$. In general, classical revivals appear for any ensemble of points having an energy distribution with sharp cutoffs (for example, a rectangular distribution). However, the two peaks evident in the energy distribution in Fig. 6 enhance the amplitudes of the revivals and decrease the rate at which they decay, which is determined by the width of each peak. These classical revivals, which result from the finite bandwidth ΔE of a continuous energy distribution, are to be distinguished from quantum revivals which are associated with the unequal spacing of the distribution of discrete energy levels.

It is interesting to analyze the degree of control that can be achieved over the localization times as well as the degree of localization by optimizing the pump pulse. Possible control parameters associated with the pump pulse are its duration, strength, rise time (t_{rise}), and fall time (t_{fall}). The sign of the pulse can be used to create wave packets moving clockwise or counterclockwise. For example, a negative (positive) value of F_z^{pump} leads to a wave packet that propagates counterclockwise (clockwise) for a pulse duration of $T_S/2$. Within the range of validity of first-order degenerate perturbation theory, the Bloch equation [Eq. (2)] remains valid for a time-dependent field $F(t)$ and thus for a time-dependent Stark frequency $\omega_S(t) = 3n_i F(t)$. The precession angle $\Delta\theta_S = \arctan[L_y/(n_i A_x)]$ [see Eq. (3)] is determined by the integral over time $\Delta\theta_S = \int[\omega_S(t)/2]dt$. To maximize $|L_y|$, pulse shapes such that $\Delta\theta_S \approx \pi/2$ must be used, which makes the eccentricity of the Kepler ellipses insensitive to the shape of $F(t)$. However, the width in energy, ΔE, of the wave packet (or phase-space distribution) depends strongly on the pulse shape as it is governed by degrees of freedom not represented by the Bloch equation. Because $H^{Stark} = H^{at} = E$ for zero field (both before and after the pump field), the pulse shape dependence of ΔE can be derived from the dynamics of the Stark interaction in Eq. (1), i.e.,

$$\frac{dH^{Stark}}{dt} = z(t)\frac{dF_z^{pump}(t)}{dt}. \tag{9}$$

For simplicity, we first consider the sudden turn on and turn off of the pump pulse, ($t_{rise} = t_{fall} = 0$). At $t = 0$, $H^{Stark} = -(2n_i^2)^{-1}$. The value of H^{Stark} for an orbit elongated along the x direction with $z \simeq 0$ remains essentially unaffected during the sudden turn on of the Stark interaction [Eq. (9)] as the latter vanishes for $z \simeq 0$. After precession the orbit encompasses a range of z coordinates and the Stark interaction becomes strongly dependent on the fall time t_{fall}. When the pump field is turned off suddenly ($t_{fall} \sim 0$) at $t = t_{off}$, i.e.,

$dF_z^{pump}(t)/dt = F_z^{pump}\delta(t-t_{off})$, and the wave packet is spread around a circular orbit [$z(t_{off}) = n^2 \sin\phi$], the final energy of a trajectory is

$$E^{sudden}(\phi) = -\frac{1}{2n_i^2} + F_z^{pump}z(t_{off}) \simeq -\frac{1}{2n_i^2} + F_z^{pump}n_i^2 \sin\phi. \tag{10}$$

The ϕ dependence of the energy, $E(\phi)$, leads to a distribution of final energies of width ΔE. The largest positive (negative) energy changes occur when $\phi = \pm\pi/2$ [i.e., $z(t_{off}) = \pm n^2$] resulting in a width,

$$\Delta E = 2|F_z^{pump}|n_i^2 \tag{11}$$

or $n_i^2 \Delta E = \Delta E_0 \simeq 2F_0 = 2n_i^4 F_z^{pump}$. The same difference in azimuthal angle, i.e., $\Delta\phi = \pi$ was used to estimate the classical revival time in Eq. (7).

This analysis can be extended to finite rise and fall times. As long as these are short compared to the Stark precession time T_S, the Kepler ellipse does not appreciably change its shape or orientation during the rise and fall times. Therefore, the final energy width can be determined from the change of H^{Stark} during the fall time $-t_{fall}/2 < (t-t_{off}) < t_{fall}/2$, i.e., integrating Eq. (9) for a trajectory on a fixed circular orbit $z(t) = n_i^2 \sin(n_i^{-3}t)$ during the fall time. In the following the fall time is defined as the time required for the amplitude of the pulse to decrease from its maximum value to zero.

Figure 7(a) illustrates the dependence of the width $\Delta\phi$ of the angular distribution on the fall time for both a linear and sinelike fall, $F(t) \propto \{1 - \sin[\pi(t-t_{off})/t_{fall}]\}$. The seemingly random dependence on t_{fall} can be accounted for by considering the induced energy spread. Figure 7(b) shows that the results for different fall times are similar when plotted as a function of $(t_0 \Delta E_0)$, the product of scaled evolution time after turn off and the scaled energy width ΔE_0. The sensitivity to t_{fall} is due to the nonmonotonic dependence of ΔE on the fall time (see Fig. 8). For a linear fall the energy width maximizes for ultrashort fall times, $t_{fall} \ll T_{n_i}$, and minimizes near multiples of the Kepler period, $t_{fall} \sim kT_{n_i}$, $k = 1,2,\ldots$. In turn, for a sinelike fall ΔE minimizes near $t_{fall} \sim (k + 1/2)T_{n_i}$. These observations follow from Eq. (9) assuming an approximately circular trajectory during the fall time. For a linear turn off

$$n_i^2 \Delta E^{linear} \simeq 2n_i^4 |F_z^{pump}| \left| \frac{\sin(\pi t_{fall}/T_{n_i})}{\pi t_{fall}/T_{n_i}} \right|, \tag{12}$$

while a sinelike turn off leads to

$$n_i^2 \Delta E^{sine} \simeq 2n_i^4 |F_z^{pump}| \left| \frac{\cos(\pi t_{fall}/T_{n_i})}{1 - (t_{fall}/T_{n_i})^2} \right|. \tag{13}$$

The time t_L at which the circular wave packet achieves maximum localization can be extended (reduced) by decreasing (increasing) the strength of the pump, $|F_z^{pump}| = \max[|F_z^{pump}(t)|]$. This results because the final energy width ΔE is linearly dependent on $|F_z^{pump}|$, i.e., $t_L \propto 1/\Delta E \propto 1/|F_z^{pump}|$. This can be seen in Fig. 9 which shows the time evolution of the angular width $\Delta\phi$ of the wave packet for
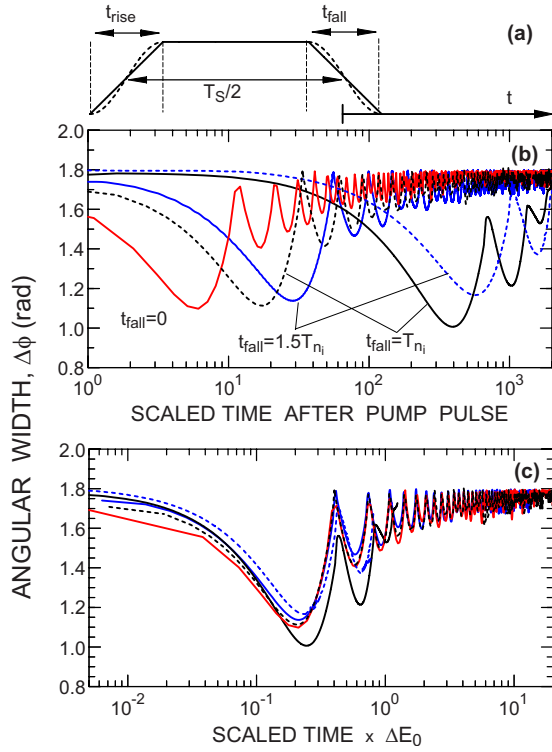
FIG. 7. (Color online) (a) Pump electric field and time scales. (b) Angular width of the wave packets created by a pump field of -10 mV cm^{-1} pulse for the different fall times indicated as a function of scaled time $[t_0 = (t - t_{off})/T_{n_i}]$, (c) same data in (b) but as a function of the scaled time multiplied by the scaled energy width of the wave packet. The solid (dashed) lines correspond to a linear (sinelike) rise and fall of the pump pulse. The curves have been smoothed by time averaging over one Kepler period. The initial state is the 1D orbit as in Fig. 1(b).

three different field strengths (1, 5, and 10 mV cm^{-1}) plotted as a function of scaled evolution time t_0 multiplied by the scaled field strength. Note that while the localization times (i.e., the times where $\langle \Delta \phi \rangle$ possesses local minima) are sensitive to t_{fall}, the functional form of the switch-off, and the strength of the pump field, the spatial width of the wave packet at the time of maximum localization is not strongly dependent on the strength of the pulse or the fall time.

One remarkable prediction contained in Fig. 8 is that under appropriate conditions both the principal action and angular momentum widths can become smaller than unity. This suggests the possibility that a classical-to-quantum crossover might be observable even at $n_i \sim 300$. Whereas classical mechanics always yields a wave packet which dephases due to a finite spread in energy, quantum mechanics would predict a nondispersive wave packet by populating only two n levels or even a stationary circular state within a single n level. This would occur when the width of the classical energy distribution is comparable to or smaller than the quantum level splitting (the Kepler frequency), i.e., $\Delta E < n_i^{-3}$. These quantum effects are different from those appearing when many energy levels are populated beyond the so-called quantum break time where classical and quantum behavior diverge. For circular wave packets the observable $\langle z(t) \rangle$ will exhibit such divergence when (full) quantum revivals appear
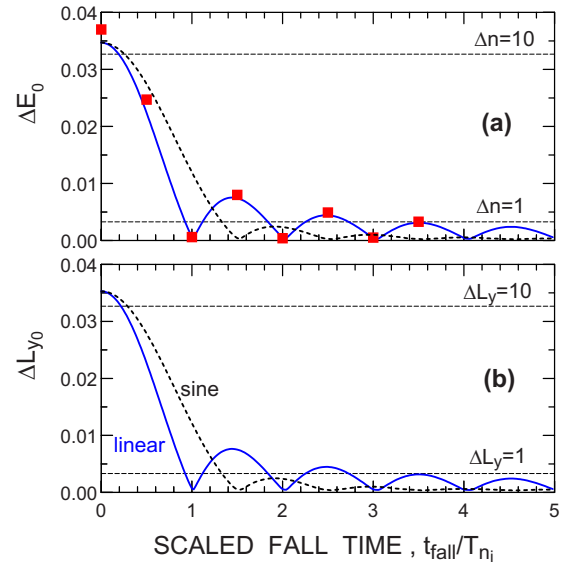
FIG. 8. (Color online) Width of the energy (a) and angular momentum (b) distributions as a function of the scaled fall time for a pump field of -10 mV cm^{-1} applied to a 1D state. The solid (dashed) lines correspond to a linear (sinelike) rise and fall of the pump pulse. The squares in (a) are for a quasi-1D state. [The large angular momentum width associated with the product state, $\Delta L_y \sim 70$, is too large to fit on the scale of (b).] The horizontal lines indicate the widths corresponding to changes of one and ten in the quantum numbers n [in (a)] and l [in (b)] for $n_i = 306$.

near $T_R \simeq n_i T_{n_i}/3$ [7,21,22]. We note that due to the symmetry of circular orbits observables such as $\langle z(t) \rangle$ barely show fractional revivals which would point to the break down of classical-quantum correspondence at earlier times. For high-n Rydberg atoms the revival time is large and is difficult to observe experimentally.
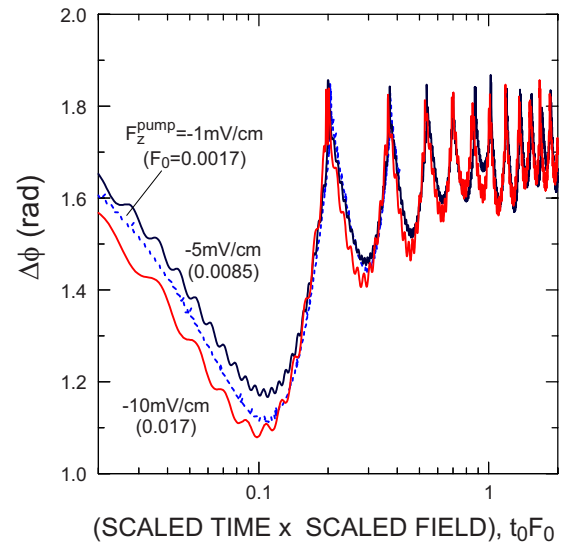
FIG. 9. (Color online) Angular width of the wave packets created by three different pump fields of -10 mV cm^{-1}, -5 mV cm^{-1}, and -1 mV cm^{-1} as a function of the scaled time $[t_0 = (t - t_{off})/T_{n_i}]$ multiplied by the scaled field $(F_0 = n_i^4 F_z^{pump})$. The pump pulse is suddenly turned on and off. The initial state is the 1D orbit as in Fig. 1(b).
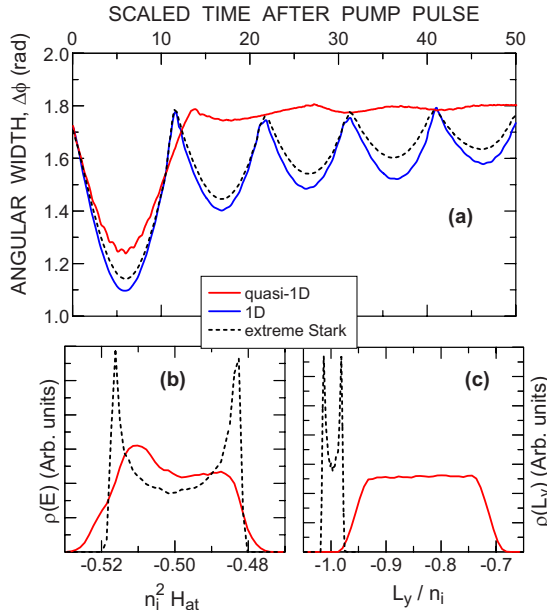
FIG. 10. (Color online) (a) Angular width of the wave packets created by sudden application and turn off of a pump field of -10 mV cm^{-1} to a 1D state, an extreme Stark state and a quasi-1D state in $n_i = 306$ (see text). The curves have been smoothed by time averaging over one Kepler period. The resulting energy and angular momentum distributions are displayed in (b) and (c), respectively.

III. EXPERIMENTAL REALIZATION

Oriented Rydberg atoms with large dipole moments can be produced by using a narrow-linewidth laser tuned to photoexcite blueshifted or redshifted states in the Stark manifold in a weak dc field. The quantum states that best approximate the linear classical 1D state discussed in the preceding section are the extreme Stark states. However, these states are difficult to produce experimentally due to the small oscillator strengths for their excitation and the small spacing between adjacent Stark states (compared to the effective laser width). Nonetheless, quasi-one-dimensional (quasi-1D) states with large dipole moments, $\langle x \rangle / n_i^2 \sim 1.25$, can be produced [14]. These states can be modeled classically using the subset of a microcanonical ensemble

$$\rho^{q1D}(\vec{r}, \vec{p}) = C \delta\left(H^{at} + \frac{1}{2n_i^2}\right) \chi_{L_x^{min}}^{L_x^{max}}(L_x) \chi_{A_x^{min}}^{A_x^{max}}(A_x), \quad (14)$$

where C is a normalization constant and χ_a^b is the characteristic function of the interval (a,b). Experimentally [14] at $n_i = 306$ photoexcitation leads to creation of an ensemble of quasi-1D states comprising of an incoherent mix of about 36 low-lying redshifted states with $-292 < n_i A_x < -220$ and $-3/2 < L_x < 3/2$. This is referred to in the following as the "quasi-1D state."

Application of a pump field to such a quasi-1D state [Fig. 10(a)] leads to the formation of a nearly circular wave packet that exhibits maximum transient localization at a time similar to that of a true 1D state. This is due to the fact that the resulting energy distributions have very similar widths [Fig. 10(b)]. However, quasi-1D states give rise to a much broader

angular momentum distribution involving ~ 70 states [Fig. 10(c)] and, consequently, much smaller classical revivals. For comparison, Fig. 10 includes results for the extreme Stark state with $-306 < n_i A_x < -304$ and $-1/2 < L_x < 1/2$ in Eq. (14). The behavior for this state is very similar to that of the 1D state. The dependence of the transient localization time for the quasi-1D state on the strength and the fall time of the pump pulse is very similar to that of the 1D state. The energy width ΔE also exhibits similar oscillatory behavior as t_{fall} is increased [see Fig. 8(a)]. The width of the angular momentum distribution remains very broad, $\Delta L_y \sim 70$, and, in contrast to the true 1D state is nearly independent of the fall time [Fig. 8(b)]. This happens because the final width ΔL_y is primarily governed by the initial L distribution of the quasi-1D state.

To experimentally test the theoretical predictions quasi-1D Rydberg atoms were formed by using an extra-cavity doubled CR699-21 Rh6G dye laser to photoexcite potassium atoms contained in a thermal-energy beam, in a weak dc field of ~ 400 μV cm^{-1} that defined the x axis along which atoms were initially oriented (see [14] for details). Photoexcitation produces an incoherent statistical mixture of ~ 36 oriented stationary Stark states with an average dipole moment $\langle x \rangle \simeq 1.25 n_i^2$ [14] and $|m| \leq 1$ in the $n_i \sim 306$ manifold (due to the ground-state hyperfine structure of potassium 75% of the laser excited atoms have $n_i = 306$ and 25% $n_i = 308$). The quasi-1D atoms were then subjected to the pump field (directed along the z axis) that was turned on rapidly, i.e., $t_{rise} \lesssim T_{n_i}$. After a predetermined time (typically $T_S/2$) the pump field was rapidly turned off ($t_{fall} \lesssim T_{n_i}$). The subsequent behavior of the wave packet was monitored using probe pulses applied along the x or z axes. The number of surviving atoms was determined by selective field ionization in which a slowly varying ramped electric field was applied to the atoms and the liberated electrons detected by a particle multiplier.

The probe pulses used to examine the spatial evolution of the wave packet were applied following a variable time delay, t_d, after turn off of the pump pulse at $t = t_{off}$. These probe pulses have short rise and fall times, ~ 0.5 ns, and a duration of 6 ns ($> T_{n_i}$). Their amplitude, 100 mV cm^{-1}, was chosen such that they typically ionized $\sim 50\%$ of the initial Rydberg atoms. The survival probability provides an indirect measure of the average electron position coordinates $x(t_{probe})$ or $z(t_{probe})$ since only those electrons with energies $H^{at} + z(t_{probe})F_z^{probe}$ [or $H^{at} + x(t_{probe})F_x^{probe}$] that lie above the top of the barrier ($-2\sqrt{|F^{probe}|}$) can be ionized [23]. As evident from Figs. 11(a) and 11(b) the measured and calculated survival probabilities are in good agreement and mirror the anticipated behavior of $\langle z \rangle$ and $\langle x \rangle$. The CTMC calculations are undertaken using fields with a sinelike fall that closely mimics the experimentally measured field profiles. The buildup of strong periodic oscillations in the survival probability and the 90° phase shift between measurements with the probe field oriented along the x and z axes confirm the production of a localized Bohr-like wave packet in near-circular orbit around the core ion. Oscillations damp after several orbits as a result of dephasing due to the distribution of excited states in the wave packet. Nonetheless, at late times (~ 35 ns) evi-
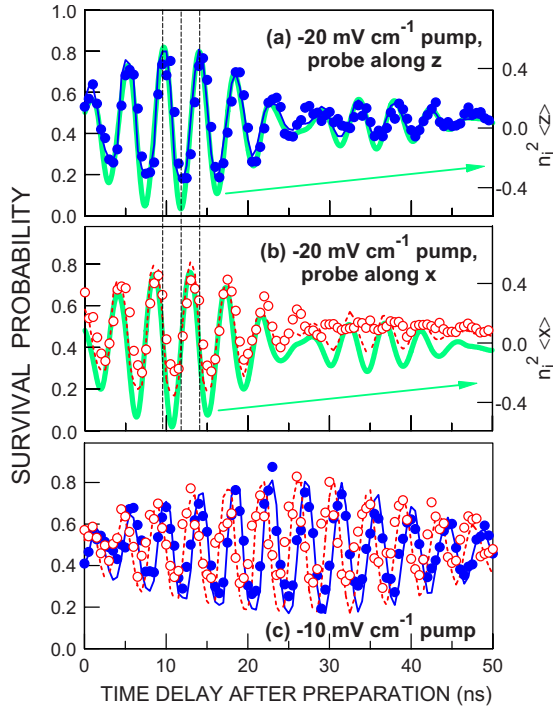
FIG. 11. (Color online) Experimental (symbols) and calculated (thin lines) survival probabilities as a function of the time delay between turn off of the pump field and application of a probe field of 6 ns duration and amplitude −100 mV cm^{-1} directed along the x and z axes. (a) F_z^{pump} = −20 mV cm^{-1} and the probe field applied along the z axis, (b) as in (a) with the probe field applied along the x axis, (c) F_z^{pump} = −10 mV cm^{-1} and probe fields applied along both the x and z axes. Also shown in (a) and (b) are the expectation values of the z and x coordinates of the wave packet (thick solid lines, right-hand axis). The vertical lines are shown to visualize the 90° phase shift between the x and z coordinates shown in (b) and (c). Both the pump pulse and the probe pulse are turned on and off suddenly.

dence of a damped classical revival is seen when probing along the z axis, although not when probing along the x axis. This discrepancy can be attributed, at least in part, to the fact that the z axis is an axis of symmetry of the apparatus whereas the x axis is not. Calculations showed that to generate pulsed fields along the x axis the associated electrode (inset in one wall of the apparatus) must be positioned off axis. The direction of the resulting field, however, is sensitive to the position of this and other electrodes. The amplitude of the variations in survival probability observed with the probe field applied along the z axis is somewhat larger than with the field applied along the x axis (see Fig. 11) suggesting that its direction might not be completely aligned with the true x axis.

Figure 11(c) shows that, as predicted, the time evolution of the survival probabilities depends sensitively on the strength of the pump field. The optimum localization times in the experiment can be inferred indirectly from the time at which the amplitude of the oscillations in survival probability are maximum (following the discussion of Figs. 2, 3, and 11). The localization times indirectly inferred from the measurements are presented in Fig. 12 and display the $1/F_z^{pump}$
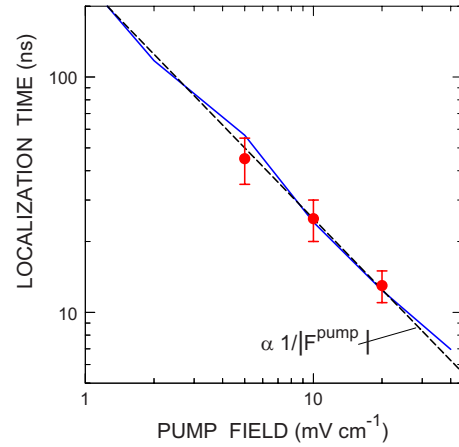
FIG. 12. (Color online) Calculated (solid line) and experimentally inferred (symbols) optimum localization times as a function of the strength of the pump pulse. Both the pump pulse and the probe pulse are turned on and off suddenly. The dashed line illustrates $1/|F_z^{pump}|$ behavior. Experimental localization times are inferred from the times at which the amplitude of the oscillations in the survival probability are maximum. The vertical error bars indicate the uncertainty in determining the maximum amplitudes. Calculated values correspond to the times at which the wave packet acquires its minimum azimuthal width.

dependence predicted by calculations of the minimum angular width. Again, the experimental data are in good agreement with CTMC simulations. As noted previously, the localization time depends sensitively on the fall time and the shape of the pump pulse. As expected, Fig. 13 shows that the measured localization times are in good agreement with
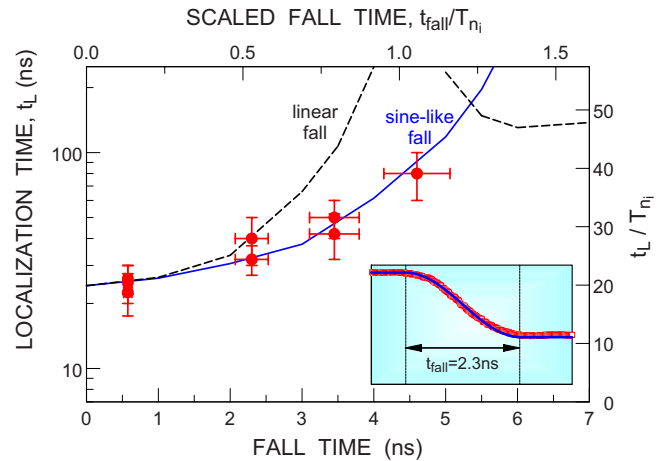
FIG. 13. (Color online) Classical maximum localization times for F_z^{pump} = −10 mV cm^{-1} as a function of the fall time of the pump pulse for a linear (dashed line) and a sinelike fall (solid line) and experimentally inferred values (symbols). The figure includes experimental data for F_z^{pump} = −5, −10, and −20 mV cm^{-1} which have been scaled to −10 mV cm^{-1} assuming a $1/|F_z^{pump}|$ behavior. The inset shows the fit (solid line) to the measured profile (symbols) obtained using the sinelike approximation for a 2.3 ns fall time (see text). The experimental fall times (from 100% to 0% of the pulse amplitude) are determined from this fit and the horizontal error bars of ±10% indicate the range of fall times that provide a good fit.

those predicted classically using a sinelike fall which, as seen in the inset, matches well the experimentally measured pulse profile.

IV. CONCLUSIONS AND OUTLOOK

A protocol has been described and experimentally realized for producing nearly circular Bohr-like wave packets. The characteristics of the wave packets can be controlled by the strength, duration, shape, and fall time of the pump pulse. The basic features of the protocol can be understood by considering the classical dynamics of a single extremely elongated ($L=0$) Coulomb orbit suddenly exposed to a transverse electric field that is maintained for one-half of a Stark period. The resulting wave packet contains two focal points that periodically overlap leading to a series of transient localization times.

A classical description should eventually fail. For the present nearly circular wave packets there might be two avenues for observing this breakdown. The first is to use longer fall times for the pump pulse such that (in this near adiabatic limit) the wave packet encompasses only one n level (i.e., $\Delta n < 1$ in Fig. 8). However, experimental studies with long fall times are difficult because laser excitation leads to two groups of atoms with different values of n_i. The second possible avenue is to reduce the rate of decoherence of the wave packet such that quantum revivals become visible [7,21]. Given that circular wave packets are relatively robust against noise, there is hope that quantum revivals might become visible even for (mesoscopic) very-high-n, $n \sim 300$, Rydberg atoms. However, this would require that the decoherence of the electronic degree of freedom be suppressed for ~ 100 orbital periods. This is challenging as it requires elimination of all stray fields including the small dc field used to create the quasi-1D states, which remains on during each experimental cycle.

The production of localized wave packets that move in nearly circular orbits might also open up an opportunity to study correlated two-electron wave packets in planetary atoms [24,25] containing an outer electron with principal quantum number n_{out} much larger than that of the inner electron, n_{in}, each far from the ground state (i.e., $n_{out} \gg n_{in} \gg 1$). The present $n \sim 306$ wave packets have an orbital period of 4.4 ns that is long enough for current laser technology to excite an inner electron whose polarization would be locked by the transient position of the outer electron and could lead to long-lived phase-locked two-electron wave packets.

[1] C. H. Cheng, C. Y. Lee, and T. F. Gallagher, Phys. Rev. Lett. **73**, 3078 (1994).

[2] J. C. Day, T. Ehrenreich, S. B. Hansen, E. Horsdal-Pedersen, K. S. Mogensen, and K. Taulbjerg, Phys. Rev. Lett. **72**, 1612 (1994).

[3] J. Hare, M. Gross, and P. Goy, Phys. Rev. Lett. **61**, 1938 (1988).

[4] R. Lutwak, J. Holley, P. P. Chang, S. Paine, D. Kleppner, and T. Ducas, Phys. Rev. A **56**, 1443 (1997).

[5] D. Delande and J. C. Gay, Europhys. Lett. **5**, 303 (1988).

[6] J. M. Raimond, M. Brune, and S. Haroche, Rev. Mod. Phys. **73**, 565 (2001).

[7] J. A. Yeazell and C. R. Stroud, Phys. Rev. Lett. **60**, 1494 (1988).

[8] R. R. Jones and L. Noordam, Adv. At., Mol., Opt. Phys. **38**, 1 (1998).

[9] A. ten Wolde, L. D. Noordam, A. Lagendijk, and H. B. van Linden van den Heuvell, Phys. Rev. Lett. **61**, 2099 (1988).

[10] F. B. Dunning, J. C. Lancaster, C. O. Reinhold, S. Yoshida, and J. Burgdörfer, Adv. At., Mol., Opt. Phys. **52**, 49 (2005).

[11] Z. D. Gaeta, M. W. Noel, and C. R. Stroud, Phys. Rev. Lett. **73**, 636 (1994).

[12] I. Bialynicki-Birula, M. Kalinski, and J. H. Eberly, Phys. Rev. Lett. **73**, 1777 (1994).

[13] J. J. Mestayer, B. Wyker, J. C. Lancaster, F. B. Dunning, C. O. Reinhold, S. Yoshida, and J. Burgdörfer, Phys. Rev. Lett. **100**, 243004 (2008).

[14] C. L. Stokely, J. C. Lancaster, F. B. Dunning, D. G. Arbo, C. O. Reinhold, and J. Burgdörfer, Phys. Rev. A **67**, 013403 (2003).

[15] M. T. Frey, F. B. Dunning, C. O. Reinhold, and J. Burgdörfer, Phys. Rev. A **55**, R865 (1997).

[16] S. Yoshida, C. O. Reinhold, J. Burgdörfer, W. Zhao, J. J. Mestayer, J. C. Lancaster, and F. B. Dunning, Phys. Rev. Lett. **98**, 203004 (2007).

[17] M. Born, *The Mechanics of the Atom* (G. Bell and Sons, London, 1926).

[18] I. C. Percival and D. Richards, J. Phys. B **12**, 2051 (1979).

[19] R. Abrines and I. C. Percival, Proc. Phys. Soc. London **88**, 861 (1966).

[20] D. G. Arbo, C. O. Reinhold, J. Burgdörfer, A. K. Pattanayak, C. L. Stokely, W. Zhao, J. C. Lancaster, and F. B. Dunning, Phys. Rev. A **67**, 063401 (2003).

[21] M. Mallalieu and C. R. Stroud, Phys. Rev. A **49**, 2329 (1994).

[22] C. O. Reinhold, J. Burgdörfer, M. T. Frey, and F. B. Dunning, Phys. Rev. A **54**, R33 (1996).

[23] B. E. Tannian, C. L. Stokely, F. B. Dunning, C. O. Reinhold, and J. Burgdorfer, Phys. Rev. A **64**, 021404(R) (2001).

[24] M. Kalinski, J. H. Eberly, J. A. West, and C. R. Stroud, Phys. Rev. A **67**, 032503 (2003).

[25] S. N. Pisharody and R. R. Jones, Science **303**, 813 (2004).